Precision synthesis and atomistic analysis of deep blue cubic quantum dots made via self-organization

Olivier Chevalier
The University of Tokyo
Takayuki Nakamuro
The University of Tokyo
Wataru Sato
The University of Tokyo
Satoru Miyashita
The University of Tokyo
Takayuki Chiba
Yamagata University
Junji Kido
Yamagata University
Rui Shang
The University of Tokyo
Eiichi Nakamura (nakamura@chem.s.u-tokyo.ac.jp)
The University of Tokyo https://orcid.org/0000-0002-4192-1741

Article

Keywords:

Posted Date: March 28th, 2022

DOI: https://doi.org/10.21203/rs.3.rs-1464874/v1

Abstract

As a crystal approaches a few nm in size, atoms become nonequivalent, bonds vibrate, and quantum effects emerge. To study quantum dots (QDs) with structural control common in molecular science, we need atomic precision synthesis and analysis. We describe here the synthesis of QDs of lead bromide perovskite via self-organization of a lead malate chelate complex and PbBr3– under ambient conditions. Millisecond and angstrom resolution electron microscopic analysis revealed the structure and the dynamic behavior of individual QDs—structurally uniform cubes made of 64 lead atoms, where eight malate molecules are located on the eight corners of the cubes, and oleylamonium cations lipophilize and stabilize the edges and faces. Lacking translational symmetry, the cube is to be viewed as a molecule rather than a nanocrystal. The QD exhibits quantitative photoluminescence and stable electroluminescence at approx. 460 nm with a narrow half-maximum linewidth of 15 nm, reflecting minimum structural defects. This controlled synthesis and precise analysis demonstrate the potential of cinematic chemistry for the characterization of nanomaterials beyond the conventional limit.

Main Text

The properties of semiconductive nanocrystals deviate from those of their bulk counterparts, the structure loses translational symmetry and quantum confinement effects result in an increased bandgap as the size approaches that of a large molecule (Fig. 1a)[1,2]. Quantum dots (QDs) are exploited for optoelectronics and quantum informatics among other applications[3,4], and are sometimes regarded as "artificial atoms" for their bound and discrete electronic states[5]. Ideally, they are to be made with sufficient size uniformity for any applications, and with precise shape control for mimicking valency and bond directionality to be used as material voxels (Fig. 1b) [6, 7, 8, 9,10, 11] or artificial nanocrystal molecules[12]. However, this stringent requirement has been more difficult to meet as the QDs become smaller[13, 14] because their synthesis has been modeled after colloid synthesis relying on hot injection methods under nitrogen[15,16]. In addition, the conventional metrics of purity assessment such as photoluminescence quantum yield (PLQY) and full width at half maximum (FWHM) are unsuitable for atomic precision analysis of individual QD particles. Inspired by recent advances in self-organization chemistry[17,18,19, 20, 21,22,23], and analysis by transmission electron microscopy (TEM) with millisecond and angstrom spatiotemporal resolution[24,25], we set two goals in this study: atomic precision synthesis via templated growth of QD particles and atomistic analysis using the single-molecule atomic-resolution time-resolved electron microscopic (SMART-EM) imaging[26].

Theory predicts blue emission of a lead bromide perovskite QD such as $Cs_{112}Pb_{64}Br_{240}$ ($Cs{\bullet}QD_4$, Fig. 1c, see Supplementary Note 1)[25]. However, in practice, previous works showed it is unstable and has poor metrics because of dangling bonds and surface defects[28] and the dynamic nature of the QD–ligand interaction[29]. We report here the synthesis of QDs of lead bromide perovskite ($MLA{\bullet}M{\bullet}QD_4$, M = Cs cation

or methylammonium ion, MA^+) at room temperature in air via self-organization of a lead malate chelate complex[30] and $PbBr_3^-$ via a corner–edge–corner intermediate similar to the one we previously described (Fig. 1d)[31]. As shown by in situ dynamic SMART-EM imaging and other analytical methods, the QD particle is a structurally uniform cube made of 4^3 Pb atoms, where eight malate molecules form a stable Pb–O chelate on the eight corners (Fig. 1e), and oleylammonium cations ($OAMH^+$) lipophilize and stabilize the edges that otherwise suffer from a large penalty of surface energy (Fig. 1f). Thus, the cube is to be viewed as a molecule of near centrosymmetry rather than a nanocrystal devoid of translational symmetry. Both MLA•MA•QD_4 (**1**) and MLA•Cs•QD_4 (**2**) exhibit deep blue photo- and electroluminescence at »460 nm with quantitative PLQY and narrow FWHM of 15 nm reflecting minimum structural defects. Thus, controlled self-assembly and SMART-EM imaging have opened a venue for synthesis and analysis of nm-sized QDs at a level of precision so far considered possible only for organic and inorganic molecules.

Carboxylic acid-enabled shape control of perovskite microcrystals

We first describe the growth of cubic microcrystals in the presence of MLA. Small crystals prefer to be spherical to minimize surface energy, and lead bromide perovskite is no exception[32]. When we quickly diluted a 1:1 dimethylformamide (DMF) solution of $PbBr_2$ and MABr with an antisolvent, toluene, a mixture of mm-size elongated dodecahedrons and cubes formed (Fig. 2a)[33]. When 0.5–4 molar equivalents of MLA per $PbBr_2$ were added to the DMF solution, only cubic crystals formed (Fig. 2b, 2c). In the presence of lactic acid or succinic acid, which share a partial structure with MLA, crystal ripening and fusion took place (Fig. 2d, 2e). Oleic acid (OA), a common acidic additive in QD synthesis, afforded entirely fused crystals, sometimes with a hint of the outline of an elongated dodecahedron (Fig. 2f). Additional images can be found in the Supplementary Information (Supplementary Fig. 2-6).

Our next task was to reduce the size from mm to nm by 10^{-9} in volume. Gibbs' classical nucleation theory tells us that reduction of the surface energy of forming crystal nuclei results in the production of more nuclei and hence reduction of their sizes[34,35]. We found that the addition of OAM dramatically reduced the QD size. With 0.15 equiv of OAM per $PbBr_2$ following the synthesis procedure for **2**, we formed a stable green-emitting colloid of QD particles of 10.6 ± 2 nm (measured on amorphous carbon, aC, using TEM) formed with an average inter-QD spacing of 1.8 nm corresponding to the length of a single molecule of OAM (Fig. 3a). With 1.5 equiv OAM, we obtained a stable colloid of blue-emitting QD particles with the size further decreased to »2.5 nm on aC (Fig. 3b). Note that saturated linear C_8, C_{12}, and C_{18} amines and benzylamine failed to produce a stable suspension in either toluene, chlorobenzene, or 1,2-dichlorobenzene. The crucial role of the *cis*-olefinic bond in OAM is therefore evident.

The photoluminescence spectra of the colloid solution of **1** are shown as a function of added OAM in Fig. 3c (the reaction terminated after 3 h at 25 °C). When we increased the amount of OAM from 0.1 to 1.0 equiv, emission at 517 nm blueshifted via bimodal emission at 0.4 equiv to exclusive emission at 453 nm with 1.0 equiv. Interestingly, we found little sign of QD_5 and QD_6 emitting at <500 nm, and instead found exclusively QD_4 emitting at 453 nm. Strong preference for the formation of QD_4 lends some credence to a growth mechanism including the tetranuclear intermediate in Fig. 1d. Fig. 3d (MLA•MA, blue line) illustrates a sudden blue shift of the emission between 0.25 and 0.5 equiv of OAM. The PLQY of emission at 453 nm reaches >95% with 1–3 equiv OAM (Fig. 3e), and FWHM remains narrow for 0.75–3 equiv of OAM (Fig. 3f). In contrast, the synthesis of OA•MA•QD_4 (**3**) made from OA instead of MLA produced much more defective QDs. As shown in Fig. 3d and 3e (black line), upon addition of 0.1 to 1.5 equiv of OAM, the emission shifted gradually from the green to the blue, and the PLQY steadily decreased after peaking at »0.7 equiv. The FWHM (Fig. 3f) first increases because of size-shifting (Fig. 3c) but then drops to below 16 nm. The OA-mediated growth went through QD_6, QD_5, and QD_4, whereas smaller QDs were clearly not favored.

We found a large difference in the kinetic profile of the growth of the blue emission between MLA- and OA-mediated synthesis (Fig. 3g, see also Supplementary Fig. 7-8). In the OA-mediated synthesis, the emission monitored at 453 nm started immediately after dilution with toluene (black curve Fig. 3g); however, in the MLA-mediated synthesis, we found a long induction time followed by a slow growth of the deep blue emission. The maximum PLQY of the rapidly grown OA•MA•QD_4 was only 24%, whereas it was >95% for MLA•MA•QD_4. The data suggest that the MLA-mediated growth went through a preequilibrium involving an intermediate that grows rapidly once formed (cf Fig. 1d).

We describe a standard procedure for the synthesis of QD_4 in the presence of MLA and OAM (Fig. 3h). $PbBr_2$, MABr, and MLA (racemic throughout this work unless otherwise noted) were dissolved in DMF to obtain a clear solution, to which OAM was added at room temperature under air (typically 30% relative humidity) with a final molar ratio of MA:Pb:Br:MLA:OAM = 1:1:3:4:1.5. OAM is protonated by MLA to form $OAMH^+$. We obtained a homogeneous white suspension by sonication. Negative ion mass spectrometric analysis of this suspension indicated that the insoluble substance consists of MLA^-, Pb•MLA^-, and $PbBr_3^-$ as dominant species (Fig. 1d). The aggregated Pb•MLA^- chelate slowly dissociated and took part in the QD formation (cf Fig. 3g, blue) upon dilution with toluene under vigorous stirring for 3 h. A slightly milky toluene solution emitting weakly at »440 nm turned gradually pale yellow, and blue emission at »453 nm gradually intensified after an »120-minute-long induction period (Fig. 3g). After 3 h, the mixture was diluted with 0.5 volume equivalent of dimethyl carbonate (DMC) and centrifuged to obtain **1** as a pale green powder with PLQY of 95.6% on average. Repeating the synthesis with CsBr

(Cs:Pb:Br:OAM = 1:1:3:1:2.3) afforded **2** emitting at 463 nm with PLQY of 97% on average after 1 h of reaction. Using d- or l-malic acid, the circular dichroism spectrum of purified **1** and **2** indicated a weak but clearly discernable Cotton effect overlapping with the major excitonic peaks (Supplementary Fig. 9), indicating that the MLA molecule is bound to the QD[36]. There was no emission of circularly polarized light.

Purity and stability of MLA•QD_4

The diameter of QD_4 measured on aC (Fig. 3b, see also Supplementary Fig. 10) showed average diameters of 2.49, 2.46, and 2.59 nm for **1**, **2**, and OA•MA•QD_4 (**3**), respectively (Fig. 4a–4c), consistent with the QD_4 structure (Fig. 1c). QD_4 accounts for 95%, 91%, but only 71% of **1**, **2**, and **3**, respectively (more in Supplementary Note 2). QD **3** was contaminated by as much as 24% of larger QDs, which is corroborated by the emission data shown in Fig. 4d–4f (see Supplementary Note 3). QD **1** and QD **2** in toluene emit at 453 and 463 nm with narrow FWHM of 14.9 and 14.7 nm, respectively. PLQY values of 95.6% and 97% are also excellent with some specimens reaching 100%. The high PLQY of **1** originates from fast radiative decay (k_r = 10.6 ´ 10^7 s^{-1}) and slow nonradiative decay (k_{nr} = 0.5 ´ 10^7 s^{-1}, see Supplementary Fig. 11 for details). The PLQY of **3** was poor and its reproducibility was low (average 24%), although FWHM at 454 nm was narrow (15 nm). The long tail toward green emission is due to contamination by QD_5 and QD_6 as shown by the red lines in Fig. 4c and 4f.

MLA•QD_4 is stable under shelf storage, UV irradiation, and electroluminescence device setup. **1** with an initial PLQY of 97% showed little sign of deterioration over 30 days under air at 5 °C in toluene containing 4 mg/mL MLA (Fig. 4g, blue triangles). It is less stable without added MLA (i.e., in pure toluene) at 5 °C (blue circles), suggesting an equilibrium that causes loss of the MLA ligand (see Supplementary Fig. 12). The half-life of **2** is much longer, approaching 40 days in pure toluene (green circles). The difference between **1** and **3** was more striking under UV irradiation (Fig. 4h). The 455-nm emission of **1** slightly decreased to 95% after 10 h, whereas that of **3** decreased quickly to half within 2 h with emission shifted to green (530 nm, indicating crystal fusion), probably because the OA ligand dissociates more easily than the multidentate MLA ligand (Supplementary Fig. 12d). Such a dissociation equilibrium also accounts for the low chemical stability of OA-based QDs. This emission shifting indicated the fusion of **3** into large nanoparticles. Both **1** and **2** showed electroluminescence (456 nm, FWHM 16.5 nm and 464 nm, FWHM 15 nm, respectively) essentially at the same wavelength as photoluminescence (455 nm, FWHM 14.9 nm and 463 nm, FWHM 14.7 nm; Fig. 4i), emitting very close to the Rec.2020 target blue on the Commission internationale de l'éclairage (CIE) 1931 chromaticity diagram (Fig. 4j). We found the stability of electroluminescence of the MLA•QDs noteworthy (Fig. 4k). QD **1** electroluminesced at 456 nm with a turn-on voltage of »6 V and continued to emit at the same wavelength even at 11 V. Similarly, **2** remained stable under the same operating conditions. The high PLQY, low k_{nr}, color purity, and stability suggest that

the MLA•QD_4 has excellent size uniformity and minimum structural defects. Taken together with the simplicity of the procedure and the mildness of the synthetic conditions, the data illustrate the advantages of the room-temperature self-organization approach for preparing structurally homogeneous ultrasmall QDs.

Locations of various groups on the QD surface

Finally, we addressed questions seldom asked in QD research on the number and location of Br atoms, MLA, and $OAMH^+$ on an individual QD_4 particle. The high purity and structural homogeneity of the isolated QD_4 particles allowed us to answer these questions using infrared (IR), energy-dispersive X-ray spectroscopy (EDX), and SMART-EM. IR analysis of a QD film on glass that was tens of nanometer thick indicated that MLA is fully deprotonated (Supplementary Fig. 13). EDX analysis of the same sample on a graphene sheet revealed the elemental composition of the QD (Fig. 5a, Supplementary Fig. 14). The first row in this figure shows a prototypical neutral QD_4, $Cs_{112}Pb_{64}Br_{240}$ (Fig. 1e). Of its 112 Cs cations, 27 are located in the crystal lattice and 85 on the surface. Among 240 Br atoms, 96 monovalent Br ions are located on the surface. The second row shows the experimental composition of MLA•Cs•QD_4 (**2**). EDX analysis revealed that it has a total of 58 Cs, hence suggesting that only 31 Cs atoms are located on the surface; that is, 5 Cs atoms on each face. It has lost 3 ± 6 surface Br atoms, and gained 9.6 ± 2 MLA molecules, suggesting that one MLA replaced one Br atom on each of the eight corners. The third row shows MLA•MA•QD_4 (**1**). It has lost 29 ± 6 surface Br atoms replaced by 9 ± 1 MLA, suggesting that one MLA acts as a tridentate ligand to replace three Br atoms on each corner[28] (cf Fig. 1d). Interestingly, the QD synthesized with 15 equiv of added OA also had 8 acid molecules/particle, suggesting that one OA anion is located also on each corner. The OA•QD_4 lacks as many as 48 Br atoms, leaving many defective Pb coordination sites.

Fig. 5b–5d summarizes the EDX data in the form of plausible models, each of which illustrates a side view of a cube. In the prototype, we find about five Cs atoms on average on four edges and a face (Fig. 5b, see Supplementary Note 1). In **2** (Fig. 5c), one Br atom on each corner is replaced by one MLA, and all Cs atoms on the edges are replaced by $OAMH^+$ so that the large penalty of surface energy on the edges in toluene is reduced through lipophilization. By assuming charge neutrality of MLA•Cs•QD_4 (**2**), we can consider that the QD was coated by 54 $OAMH^+$, corresponding to a density of 1.5 $OAMH^+$ nm^{-2}, in good agreement with the density (1.2–1.5 $OAMH^+$ nm^{-2}) previously reported[37]. In **1** (Fig. 5d), three Br atoms on each corner are replaced by one MLA.

The SMART-EM cinematographic imaging on an aberration-corrected TEM equipped with cameras operating at 50–200 frames per second (fps) provided experimental support for the models in Fig. 5c and 5d. To this end, we decorated an aggregate of carbon nanotubes (CNTs) with 1,3,5-benzenetricarboxylic acid used as a "chemical fishhook[22]," on which we captured individual QDs from toluene solution (Fig. 5e). Without the fishhook installed, we could not capture any QDs. Note that the sizes of the atomic images are approximately proportional to $Z^{2/3}$ (Z = atomic number), and we can see using TEM only the heavy atoms, Br (Z = 35), Cs (55), and Pb (82) atoms, but not C, N, and H atoms. A Z-correlated (ZC) model is shown in Fig. 5K[38].

Fig. 5f–5j shows a series of 20-millisecond video frames (50 fps) of **2** partially exposed to vacuum. It is partially buried in an electron-rich and conductive CNT substrate (»10^3 more conductive than aC) that protects the specimen from radiolysis[39]. The cube was structurally stable over 27 s, although it tumbled a few times possibly on the fishhook serving as a pivot (Fig. 5e) because of stochastic motions of the CNT substrate[40]. The slightly blurred image of individual atoms reflects atomic vibration during the 20-millisecond imaging period (Fig. 5f–5j). In these figures, we can identify three edges, two faces, and three corners, from which we determined the geometrical orientation of the cuboid along the electron beam. The ZC structural model of $Cs_{58}Pb_{64}B_{240}^{54-}$ in Fig. 5k is seen from the same direction. In this model, the surface is fully Br passivated except that the edge Br (#1 in Fig. 5k) is replaced by MLA and not seen. The TEM image and the model share several common features: eight parallel arrays of heavy atoms as counted from the edge in the center (line 1 shown in Fig. 5i, 5k), rhombic lattice images due to Pb and Br (blue broken lines in Fig. 5k), and, importantly, the lack of Cs atoms in all edges (compare Fig. 5b and 5c). Note that the Cs atoms should have been seen clearly if they were present on the edges. This provides an atomistic proof of the lack of surface defects that was suggested from the excellent PLQY and high stability. A 0.6–0.7 nm Pb–Pb distance determined for the rhombic lattice image agrees with the »0.6 nm distance in a bulk crystal of $CsPbBr_3$, considering the lattice vibration and instrumental resolution of 0.08 nm (see Supplementary Information for details). Fast Fourier transform analysis of the whole area of the QD image indicated that the specimen is structurally homogeneous (Supplementary Fig. 18-19).

A 5.0-millisecond snapshot of an MA•QD is shown in Fig. 5l[41]. Individual atoms are seen clearly except those blurred on the edge in the middle, suggesting a motion localized along the edge. Comparison with $Cs•QD_4$ **2** in Fig. 5i suggests that more than one Br atom, possibly three atoms, are lost from the corner as expected from the EDX data (Fig. 5d). The 13.3-millisecond video images of **1** shown in Fig. 5m, 5n are more blurred than the 20-millisecond images of **2**, hence suggesting higher flexibility of the lattice of **1**. These images also support the loss of more than one Br atom from the corner. The outline of the two edges is less uniform than that of the Cs QD, and the several dots due to Br atoms moved during 26.6 milliseconds (yellow arrows). The observed difference between the MA and Cs perovskite agrees with the liquid-like property of the former previously found for bulk materials[42].

Conclusion

In summary, we have synthesized defect-free lead bromide QD_4 emitting at »460 nm, formed under the MLA/OAM-mediated self-organization conditions, and determined the structure of individual QD particles including the locations of bromine, cesium, carboxylate, and $OAMH^+$ groups on the QD surface—structural information much sought after in this field of research. The key synthetic feature includes template growth with corner and edge stabilization by MLA and $OAMH^+$, which resulted in nearly exclusive formation of QD_4 of high structural purity. The key analytical technology includes the SMART-EM imaging of individual QD particles captured on a "chemical fishhook," which provided information hitherto unavailable by a conventional method including dynamics of ligand coordination on individual QD particles revealed with millisecond and angstrom spatiotemporal resolution. The work illustrates the potentiality of cinematic chemistry for the exploration of chemistry and materials science beyond the conventional limit[43].

Methods

General

Chemicals were purchased from Tokyo Kasei Co., Aldrich Inc., and other commercial suppliers and used after appropriate purification before use. Anhydrous toluene was purchased from KANTO Chemical Co., Inc. and purified prior to use by a solvent purification system (GlassContour) equipped with columns of activated alumina and supported copper catalyst. The water content of solvents was confirmed to be less than 30 ppm by Karl-Fischer titration performed with MKC-210 (Kyoto Electronics Manufacturing Co., Ltd.). A black powder of aggregate of conical carbon nanotubes (CNT) was purchased from NEC Co. (Carbon Nanohorns (CNHs), Lot No. 181-3-2; assay: 90%) and used as purchased. Distilled water was further purified with Millipore Milli-Q (Milli-Q Reference, Merck). TEM grid precoated with a lacy microgrid NS-C15 (pore size 3 – 8 mm, carbon film thickness < 10 nm) and SHR-C075 (carbon film thickness < 6 nm) were purchased from Okenshoji Co., Ltd.). Aggregate of aminated-CNT was prepared according to reported procedure[44].

$MAPbBr_3$ microcrystal synthesis

The synthesis is based on a ligand-assisted reprecipitation strategy (LARP). To 29.4 mg of $PbBr_2$, 9.0 mg of methyl ammonium bromide (MABr) and 2 mL of dimethylformamide (DMF) were added to form a 40 mmol/mL solution (MA:Pb = 1:1). Malic acid or other acids were then added, and the mixture was stirred for 10 minutes at rt until a clear solution is obtained. 250 mL of the resulting clear solution were quickly added to 8 mL of toluene under vigorous stirring and a bright orange precipitate immediately formed. After a few seconds at rt under ambient conditions (20 °C / 30% humidity), 2mL of the solution were deposited on a thin semiconductive graphite sheet on duct-tape for SEM observations.

Quantum dot (QD) synthesis

The synthesis is based on a LARP strategy.

MLA•MA•QD_4 **(1)**

To 29.4 mg of $PbBr_2$, 9.0 mg of methyl ammonium bromide (MABr) and 2 mL of dimethylformamide (DMF) were added to form a 40 mmol/mL solution (MA:Pb = 1:1). Malic acid (MLA, 43.0 mg, 4 equiv) was then added and the mixture stirred for 10 minutes at rt until a clear solution is obtained. Then, oleylamine (OAM, 39.6 mL, 1.5 equiv) was added to the clear solution and a white precipitate formed. Then, the solution was sonicated until it became a homogenously white suspension (~5 minutes). The resulting white precursor solution was slowly (one droplet every 6 seconds, 250 mL in total) added to 8 mL of toluene under vigorous stirring. The solution was then stirred for 3 h at rt under ambient conditions (20 °C / 30% humidity) and the solution gradually changed color, from clear to pale yellow. The resulting crude was centrifugated at 10,000 rpm for 10 minutes and the precipitate was discarded. Isolated QDs (solid) was obtained after precipitation by using 0.5 volume equivalents of dimethyl carbonate (DMC) as a washing solvent immediately followed by centrifugation at 12,000rpm for 12 minutes (Fig. 3h in main text). These QDs were dispersed in toluene for further analysis, or in heptane (3.0 mg/mL) for device fabrication.

MLA•Cs•QD_4 **(2)**

To 15 mg of $PbBr_2$, 8.7 mg of CsBr and DMF (1 mL) were added to form a 40 mmol/mL solution (Cs:Pb = 1:1). 1 equiv of MLA (5.4 mg) was added to the solution and the mixture was stirred for 45 minutes at rt to give a clear solution. OAM (30 mL, 2.3 equiv) was added to the clear solution and a thick white precipitate formed. Then, the solution was sonicated until it became a homogenously white suspension (15~20 minutes). The resulting white precursor solution was slowly (one droplet every 6 seconds, 250 mL in total) added to 8 mL of toluene under vigorous stirring. The solution was then let to stir for 50 minutes at rt under ambient (20 °C / 30% humidity) and the solution gradually changed color, from clear to a cloudy pale green~yellow solution. The resulting crude was centrifugated at 12,000 rpm for 15 minutes and the precipitate was discarded. Isolated QDs (solid) could be obtained after precipitation by using 0.5 volume equivalents of DMC as a washing solvent immediately followed by centrifugation at 7,000rpm for 15 minutes. These QDs were dispersed in toluene for further analysis, or in heptane (3.0 mg/mL) for device fabrication.

OA•MA•QD_4 **(3)**

To 29.4 mg of $PbBr_2$, 9.0 mg of MABr and DMF (2 mL) were then added to form a 40 mmol/mL solution (MA:Pb = 1:1). OA (379 mL, 15 equiv) and OAM (53 mL, 2 equiv) were added. The resulting clear precursor solution (100 mL) was added to 5 mL of toluene under vigorous stirring. The solution was then let to stirred for 3 h at rt under ambient (20 °C / 30% humidity) and the solution gradually changed color, from clear to orange. The resulting crude was centrifugated at 10,000 rpm for 10 minutes and the precipitate was discarded. Isolated QDs (solid) was obtained after precipitation by using 0.5 volume equivalents of DMC as a washing solvent immediately followed by centrifugation at 15,000rpm for 20 minutes.

SEM instrumentation and sampling

Scanning electron microscopy (SEM) observations were performed on FEI Magellan 400L at $5 \acute{} 10^{-5}$ Pa. SEM analysis was carried out at 3 ~ 6 kV beam acceleration, 13 ~ 25pA and a 2 mm working distance. SEM-EDX analysis was performed on AMETEK/EDAX Genesis APEX4 at working distance was set to 4.0 mm and at a beam acceleration voltage to 3 kV. EDX analysis was averaged over 20 measurements. Both SEM and SEM-EDX samples were prepared by dropping 20 mL of sample solution in toluene on a thin graphite layer.

Spectroscopic instrumentation

UV-Vis absorption spectra in toluene were measured with a JASCO V-670 spectrometer. Fluorescence spectra were obtained on a JASCO FP-8500 spectrometer. Excitation was set at 372 nm. Kinetic studies were carried out at a fixed 20 °C in a JASCO FP-8500 equipped with a stirrer by taking a fluorescence spectrum every 4 minutes over the course of the reaction. Circular dichroism (CD) spectra were measured on a JASCO J-1500 spectropolarimeter. Electroluminescence characteristics were measured under ambient conditions using a Konica-Minolta CS2000. Quantum yields were evaluated using the relative comparative method. 9,10-diphenylanthracene was used as a standard (97% QY in the blue in cyclohexane[45]) in the formula:

$$\Phi_{sample} = \Phi_{standard} \frac{m_{sample}}{m_{standard}} \left(\frac{n_{sample}}{n_{standard}}\right)^2$$

With Φ the quantum yield, m the gradient of the plot integrated fluorescence intensity against absorbance and n the refractive index of the solvent ($n_{Cyclohexane}$ = 1.4265, $n_{Toluene}$ = 1.4969), for the sample and the standard, respectively.

Fluorescence lifetimes were measured on Hamamatsu Photonics C11367-02 Quantaurus-Tau. The radiative and nonradiative rate constants k_r and k_{nr} are calculated by substituting fluorescence quantum

yield Φ and fluorescence lifetime t for the following formula:

$$k_r = \frac{\Phi}{\tau} \qquad k_{nr} = \frac{1-\Phi}{\tau}$$

Device fabrication

LED with MLA•MA•QD_4 **(1)**

Pre-patterned indium tin oxide (ITO)-coated glass substrates were cleaned using sonication in water, soapy water and isopropanol for 10 min, respectively. The substrates were dried with a nitrogen blowgun, followed by ultraviolet ozone treatment (Sen Lights, PL16-110). PEDOT:PSS (Clevios PVP AI 4083) was filtrated through 0.45 mm PVDF and spin-coated onto the ITO-coated glass substrates at 4,000 rpm for 30 s and was annealed at 120 °C for 10 min. Poly-TPD was spin-coated from chlorobenzene (CB) solution (8 mg mL^{-1}) at 4,000 rpm for 30 s after filtration through 0.45 mm PTFE and was annealed at 120 °C for 10 min. The substrates were transferred in a nitrogen filled glovebox. The QDs were spin-coated from heptane (filtrated through 0.25 mm PTFE, 3 mg mL^{-1}) at 2,000 rpm for 30 s and were annealed at 70 °C for 3 min. TPBi in ethyl acetate (3.5 mg mL^{-1}) was sequentially spun at 2,000 rpm for 20 s and 4,000 rpm for 20 s and annealed at 70 °C for 3 min. Finally, Ag (100 nm) was evaporated through a shadow mask under high vacuum (<10^{-4} Pa).

LED with MLA•Cs•QD_4 **(2)**

Pre-patterned indium tin oxide (ITO)-coated glass substrates were cleaned using sonication in water, soapy water and isopropanol for 10 min, respectively. The substrates were dried with a nitrogen blowgun, followed by ultraviolet ozone treatment. PEDOT:PSS was filtrated through 0.45 mm PVDF and spin-coated onto the ITO-coated glass substrates at 4,000 rpm for 30 s and was annealed at 120 °C for 10 min. Poly-TPD was spin-coated from CB solution (8 mg mL^{-1}) at 4,000 rpm for 30 s and was annealed at 120 °C for 10 min. The substrates were transferred in a nitrogen filled glovebox. The QDs were spin-coated from heptane (filtrated through 0.25 mm PTFE, 3 mg mL^{-1}) at 2,000 rpm for 30 s. Finally, TPBi (30 nm) and Ag (100 nm) were evaporated through a shadow mask under high vacuum (<10^{-4} Pa).

TEM instrumentation

Atomic-resolution transmission electron microscopic (TEM) observation was carried out on a JEOL JEM-ARM200F instrument equipped with an aberration corrector (point resolution: 0.10 nm) at 298 K and at an acceleration voltage of E = 80 kV, under 1 ´ 10^{-5} Pa in the specimen column. We used a spherical

aberration (C_s) value of between 1 and 3 µm, and an electron dose rate (EDR; the number of electrons per second per nm^2) of 3.0 ´ 10^5 – 3.0 ´ 10^7 e^- nm^{-2} s^{-1} at ´ 2,000,000 magnification. A series of images were continuously recorded at a frame rate of 50 fps or 75 fps (frame per second) on a CMOS camera (Gatan OneView, In situ mode, D-mode, 4096 ´ 4096 pixels) operating on a binning 4 mode (output image size: 1024 ´ 1024 pixels, pixel resolution 0.021 nm at ´ 2,000,000) or 8 mode (output image size: 512 ´ 512 pixels, pixel resolution 0.042 nm at ´ 2,000,000). For imaging at 200 fps, OneView-IS I-mode operating on a binning 4 mode (output image size: 1024 ´ 1024 pixels, pixel resolution 0.021 nm at ´ 2,000,000). All images were automatically processed on a Gatan DigitalMicrograph software. To record the atomic-resolution movies of the specimens, we first surveyed the whole areas on the grid at low magnification to find specimens suitable for careful analysis. To analyze them in depth, we increased the magnification and started the recording. The images were recorded at under-focus conditions (defocus value: 3 – 10 nm). The images were recorded in a .dm4 format using the Gatan DigitalMicrograph software and were transformed into 8-bit or 32-bit .tiff format file by Fiji software[46]. All imaged were filtered by a bandpass filter (filtering structures smaller than 0 – 3 pixels and larger than 40 pixels, tolerance of direction: 5%).

Preparation of TEM grids for statistical analyses

The toluene solution of QDs (blue and green) at the 1 mg/mL concentration (10 µL) was drop casted onto a SHR-C075 microgrid placed on a paper that absorbed excess toluene. The resulting TEM grid was placed in vacuo (60 Pa) at 298 K for 1 hour. Statistical analyses were performed immediately after preparation of TEM grids.

Modeling and TEM image simulation

Each experimental TEM image was analyzed through comparison with the simulated images of putative models of QDs seen from various directions. To create the model, it is necessary to determine the angles of observation from the experimental TEM images of QDs that are inclined in three dimensions. The tilts of QDs were calculated mathematically using the two clearly observed edges and the central line. The structure of QDs for the modeling was generated on a Materials Studio software by using reported structural data (CCDC 1446529 for $MAPbBr_3$, mp-600089 for $CsPbBr_3$). Additional models were designed on Blender v.2.93.5.

Preparation of the fishhook for QDs analyses (Fig. 5e)

Tris(2,5-dioxopyrrolidin-1-yl) benzene-1,3,5-tricarboxylate[47] (4.2 mg, 8.4 µmol, 10 equiv vs. -NH_2 on CNT) was mixed with a powder of aminated CNT (0.167 µmol/ mg of -NH_2 groups, 5.0 mg) in 1 mL of

DMF/H_2O (1:1, v/v) in a two-necked flask. After stirring at room temperature for 24 hours, LiOH•H_2O (1.8 mg, 50 equiv vs. -NH_2 groups) was added to the mixture and stirred for another 24 hours. 1 M HCl (2.0 mL) was then added to the mixture and stirred for 5 min. The resulting suspension was filtered through a PTFE membrane filter (ADVANTEC, pore size: 100 nm) and washed with H_2O (1 mL × 3), DMF (1 mL × 3) and Et_2O (1 mL × 3), to obtain 9.2 mg of the fishhook as a black powder after vacuum drying (60 Pa) for 12 hours.

Preparation of TEM samples for atomistic analyses of QDs

The fishhook (0.5 mg) was added to the Schlenk tube and heated at 120 ℃ under vacuum for 2 hours. After thorough drying the sample and cooled to the room temperature, its atmosphere was exchanged to nitrogen and QDs solution was added to the tube. After stirring it for 24 hours, the reaction mixture was filtered through a PTFE membrane filter (ADVANTEC, pore size: 0.2 μm) and a black filter cake was washed with dried toluene (1 mL ´ 3) under nitrogen flow. The black powder was placed in vacuo (60 Pa) for 1 hour to obtain the sample for TEM (0.45 mg). The black powder of QDs@-CNT forming a large agglomerate was dispersed in toluene (2 mL/mg) under nitrogen flow, and gently ground for 3 minutes in an agate mortar so as to break the agglomerate into individual CNT aggregates for TEM analysis. The dispersion was filtered through Kiriyama 5A filter (pore sizes: 7 μm), and the filtrate (10 μL) was drop casted onto a TEM microgrid (NS-C15) placed on a paper that absorbed excess toluene. The resulting TEM grid was placed in vacuo (60 Pa) at room temperature for 1 hour, which was analyzed by single-molecule atomic-resolution time-resolved electron microscopy (SMART-EM).

Using the same conditions, we could not capture QDs on the surface of single-wall CNT (Meijo Arc SO, produced by arc-discharge using Ni and Y catalysts, >90% purity, average diameter 1.4 nm, Lot #1908222), carbon nanohorn (as prepared), nor oxidized carbon nanohorn (treated at 550 ℃ under O_2 atmosphere).

References

1 Brus, L. Electronic wave functions in semiconductor clusters: experiment and theory. J. Phys. Chem. 90, 2555–2560 (1986).

2 Shamsi, J., Urban, A. S., Imran, M., De Trizio, L. & Manna, L. Metal Halide Perovskite Nanocrystals: Synthesis, Post-Synthesis Modifications, and Their Optical Properties. Chem. Rev. 119, 3296–3348 (2019).

3 Ladd, T. D. et al. Quantum Computers. Nature 464, 45–53 (2010).

4 Liu, K., Jiang, Y., Guo, Y., Liu, Y. & Nakamura, E. Chemical Formation and Multiple Applications of Organic–Inorganic Hybrid Perovskite Materials. J. Am. Chem. Soc. 141, 1406–1414 (2019).

5 Banin, U., Cao, Y., Katz, D. & Millo, O. Identification of atomic-like electronic states in indium arsenide nanocrystal quantum dots. Nature 400, 542–544 (1999).

6 Talapin, D. V. et al. Quasicrystalline order in self-assembled binary nanoparticle superlattices. Nature 461, 964–967 (2009).

7 Auyeung, E. et al. Synthetically programmable nanoparticle superlattices using a hollow three-dimensional spacer approach Nat. Nanotechnol. 7, 24–28 (2012).

8 Ross, M. B. et al. Nanoscale form dictates mesoscale function in plasmonic DNA-nanoparticle superlattices. Nat. Nanotechnol. 10, 453-458, (2015).

9 Garcia-Lojo, D., et al. Plasmonic Supercrystals. Acc. Chem. Res. 52, 1855–1864 (2019).

10 Laramy, C. R., O'Brien, M. N. & Mirkin, C.A. Crystal engineering with DNA. Nat. Rev. Mater. 4, 201–224 (2019).

11 Baek, W. et al. Highly luminescent and catalytically active suprastructures of magic-sized semiconductor nanoclusters. Nat. Mater. 20, 650–657, (2021).

12 Choi, C. A. & Alivisatos, A. P. From Artificial Atoms to Nanocrystal Molecules: Preparation and Properties of More Complex Nanostructures. Annu. Rev. Phys. Chem. 61, 369–389 (2010).

13 Li, J., Fang, Z., He, H. & Ye, Z. Bright Tail States in Blue-Emitting Ultrasmall Perovskite Quantum Dots. J. Phys. Chem. Lett. 8, 6002–6008 (2017).

14 Rossi, D. et al. Light-Induced Activation of Forbidden Exciton Transition in Strongly Confined Perovskite Quantum Dots. ACS Nano 12, 12436–12443 (2018).

15 Protesecu, L. et al. Nanocrystals of Cesium Lead Halide Perovskites (CsPbX3, X = Cl, Br, and I): Novel Optoelectronic Materials Showing Bright Emission with Wide Color Gamut. Nano Lett. 15, 3692–3696 (2015).

16 Kwon, S. G. & Hyeon, T. Formation Mechanisms of Uniform Nanocrystals via Hot-Injection and Heat-Up Methods. Small 7, 2685–2702 (2011).

17 Xu, W. et al. Anisotropic reticular chemistry. Nat. Rev. Mater. 5, 764–779 (2020).

18 Boles, M. A., Engel, M. & Talapin, D. V. Self-Assembly of Colloidal Nanocrystals: From Intricate Structures to Functional Materials. Chem. Rev. 116, 112200–11289 (2016).

19 Raino, G. et al. Superfluorescence from lead halide perovskite quantum dot superlattices. Nature 563, 671–675 (2018).

20 Kovalenko, M. V. Opportunities and challenges for quantum dot photovoltaics. Nat. Nanotechnol. 10, 994-997, (2015).

21 Hanikel, N., Prévot, M. S., Yaghi, O. M., MOF water harvesters. Nat. Nanotechnol. 15, 348-355, (2020).

22 Van Zee, N. J. et al. Potential enthalpic energy of water in oils exploited to control supramolecular structure. Nature 558, 100–103 (2018).

23 Fujita, M., Tominaga, M., Hori, A. & Therrien, B. Coordination Assemblies from a Pd(II)-Cornered Square Complex. Acc. Chem. Res. 38, 369–378 (2005).

24 Xing, J., Schweighauser, L., Okada, S., Harano, K. & Nakamura, E. Atomistic structures and dynamics of prenucleation clusters in MOF-2 and MOF-5 syntheses. Nat. Comm. 10, 3608 (2019).

25 Nakamuro, T., Sakakibara, M., Nada, H., Harano, K. & Nakamura, E. Capturing the Moment of Emergence of Crystal Nucleus from Disorder. J. Am. Chem. Soc. 143, 1763–1767 (2021).

26 Nakamura, E. Atomic-Resolution Transmission Electron Microscopic Movies for Study of Organic Molecules, Assemblies, and Reactions: The First 10 Years of Development. Acc. Chem. Res. 50, 1281–1292 (2017).

27 Galkowski, K. et al. Determination of the exciton binding energy and effective masses for methylammonium and formamidinium lead tri-halide perovskite semiconductors. Energy Environ. Sci. 9, 962–970, (2016).

28 Dey, A. et al. State of the Art and Prospects for Halide Perovskite Nanocrystals. ACS Nano 15, 10775–10981 (2021).

29 De Roo, J. et al. Highly Dynamic Ligand Binding and Light Absorption Coefficient of Cesium Lead Bromide Perovskite Nanocrystals. ACS Nano 10, 2071–2081 (2016).

30 Ghosh, A. & Rao, C. N. R. Chiral and Achiral Malate Frameworks with Different Dimensionalities. Z. Anorg. Allg. Chem. 634, 1115–1122 (2008).

31 Guo, Y. et al. Chemical Pathways Connecting Lead(II) Iodide and Perovskite via Polymeric Plumbate(II) Fiber. J. Am. Chem. Soc. 137, 15907–15914 (2015).

32 Feng, A. et al. Shape Control of Metal Halide Perovskite Single Crystals: From Bulk to Nanoscale. Chem. Mater. 32, 7602–7617, (2020).

33 Guo, Y. et al. Citric Acid Modulated Growth of Oriented Lead Perovskite Crystals for Efficient Solar Cells. J. Am. Chem. Soc. 139, 9598–9604 (2017).

34 Vekilov, P. G. Nucleation. Cryst. Growth Des. 10, 5007–5019 (2010).

35 Li, Z., Saruyama, M., Asaka, T., Tatetsu, Y. & Teranishi, T. Determinants of crystal structure transformation of ionic nanocrystals in cation exchange reactions. Science 373, 332–337 (2021).

36 Tohgha, U. et al. Ligand Induced Circular Dichroism and Circularly Polarized Luminescence in CdSe Quantum Dots. ACS Nano 7, 11094–11102 (2013).

37 Smock, S. R., Williams, T. J. & Brutchey, R. L. Quantifying the Thermodynamics of Ligand Binding to CsPbBr3 Quantum Dots. Angew. Chem. Int. Ed. 57, 11711–11715 (2018).

38 Xing, J. et al. Atomic-Number (Z)-Correlated Atomic Sizes for Deciphering Electron Microscopic Molecular Images. arXiv:2107.01490 (2022).

39 Liu, D. et al. Ionization and electron excitation of fullerene molecules in a carbon nanotube. A variable temperature/voltage transmission electron microscopic study. arXiv:2110.02530 (2022).

40 Shimizu, T. et al. Real-Time Video Imaging of Mechanical Motions of a Single Molecular Shuttle with Sub-Millisecond Sub-Angstrom Precision. Bull. Chem. Soc. Jpn. 93, 1079–1085 (2020).

41 Zhang, D. et al. Atomic-resolution transmission electron microscopy of electron beam–sensitive crystalline materials. Science 359, 675–679 (2018).

42 Zhu, X. Understanding lead halide perovskites. J. Chem. Phys. 153, 030401, (2020).

43 Keinan, E. A Scientist and a Musician. AsiaChem. 2, 96–103, (2021).

Supplementary References

44 Hanayama, H., Yamada, J., Harano, K. & Nakamura, E. Cyclodextrins as surfactants for solubilization and purification of carbon nanohorn aggregates. Chem. Asian J. 15, 1549–1552 (2020).

45 Brouwer, A. M. Standards for photoluminescence quantum yield measurements in solution (IUPAC Technical Report). Pure Appl. Chem. 83, 2213–2228 (2011).

46 Schindelin, J. Fiji: an open-source platform for biological-image analysis. Nat. Methods 9, 676–682 (2012).

47 Megens, R. P., Van den Berg, T. A., de Bruijn, A. D., Feringa, B. L. & Roelfes, G. Multinuclear Non-Heme Iron Complexes for Double-Strand DNA Cleavage. Chem. Eur. J.

48 Ten Brinck, S. & Infante, I. Surface Termination, Morphology, and Bright Photoluminescence of Cesium Lead Halide Perovskite Nanocrystals. ACS Energy Lett. 1, 1266-1272 (2016).

49 Ravi, V. K. et al. Origin of the Substitution Mechanism for the Binding of Organic Ligands on the Surface of CsPbBr3 Perovskite Nanocubes. J. Phys. Chem. Lett. 8, 4988-4994 (2017).

50 Galkowski, K. et al. Determination of the exciton binding energy and effective masses for methylammonium and formamidinium lead tri-halide perovskite semiconductors. Energy Environ. Sci. 9, 962-970 (2016).

51 Oomens, J. & Steill, J. D. Free Carboxylates Stretching Modes. J. Phys. Chem. A 112, 3281-3283 (2008).

Declarations

Acknowledgments: We thank Prof. Koji Harano, Dr. Ryosuke Sekine, Mrs. Hinako Ebe for helpful discussion. We thank Mitsubishi Chemical Corporation for partial financial support. This research is supported by MEXT KAKENHI grant number 19H05459, JSPS KAKENHI 20K15123. O.C. thanks the Program of Excellence in Photon Science for a predoctoral fellowship.

Author contributions: E.N. R.S. and T.N. guided the research and wrote the manuscript with O.C. O.C. performed the experiments with assistance from W.S., S.M., T.C., and J. K.; E.N. R.S. and O.C. developed the QD synthesis. T.N. carried out the TEM experiments and analyzed the experimental data with O.C., R.S., and E.N.; All authors contributed to designing the experiments, analyzing the data and editing the manuscript.

Competing interests: E.N., R.S., O.C., W.S. are inventors on Japanese patent application number 2020-156302, submitted by The University of Tokyo, which covers synthetic methods described in this manuscript. T. N., S. M., T.C., J. K. declare no competing interests.

Data and materials availability: Supplementary information is available for this paper.

Corresponding authors: Correspondence and requests for materials should be addressed to T.N. (muro@chem.s.u-tokyo.ac.jp), R.S. (rui@chem.s.u-tokyo.ac.jp), E. N. (nakamura@chem.s.u-tokyo.ac.jp)

Figures

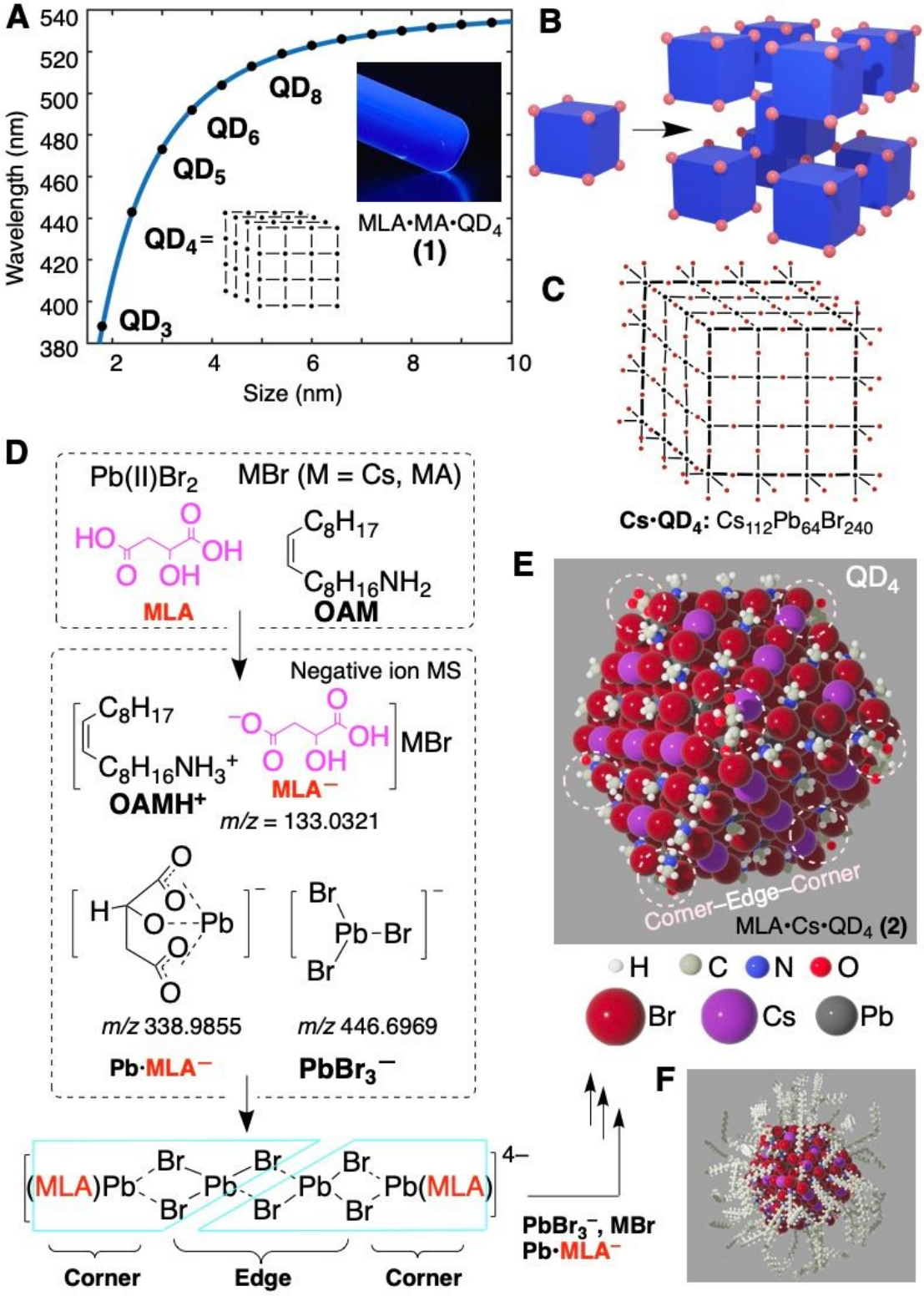

Figure 1

Synthesis of lead perovskite QD made of 4^3 Pb atoms stabilized by MLA and OAM. a, Size/wavelength correlation for methylammonium lead perovskite QD_n according to the Brus equation with effective mass approximation[27]. The subscript n refers to the number of Pb atoms on an edge. **b**, Cubic voxel and 3-D assembly. **c**, $Cs_{112}Pb_{64}Br_{240}$ ($Cs•QD_4$). All Cs and most of the Pb (black) and Br (red) are omitted for

clarity. **d**, Self-organization of $PbBr_2$, MBr, MLA, and OAM into a corner–edge–corner constituent of MLA•Cs•OD_4 (**2**), and intermediates detected using negative ion mass spectrometry (Supplementary Fig. 1). **e**, A 3-D picture of **2**, where $OAMH^+$ is simplified as MA^+ for clarity. MLA molecules are circled. **f**, **2** with $OAMH^+$ molecules shown.

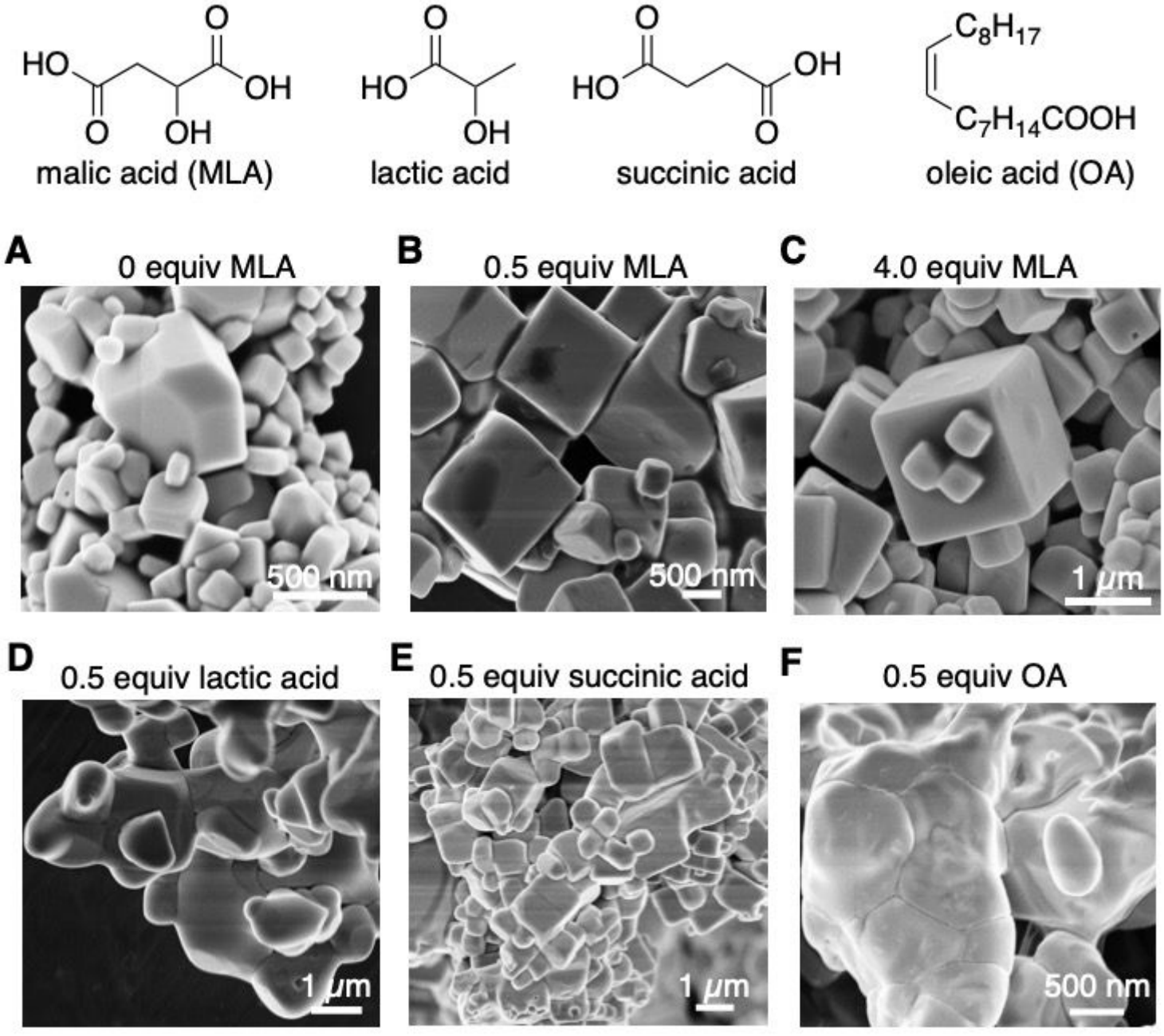

Figure 2

Dependency of shape and size of microcrystals of methylammonium lead perovskite on added carboxylic acids. Experiments were performed under the standard conditions of the QD synthesis, in which MLA was replaced by the acid shown and no oleylamine was added to promote unrestricted

growth. **a**, No MLA. **b**, 0.5 equiv MLA. **c**, 4.0 equiv MLA. **d**, 0.5 equiv lactic acid. **e**, 0.5 equiv succinic acid. **f**, 0.5 equiv OA.

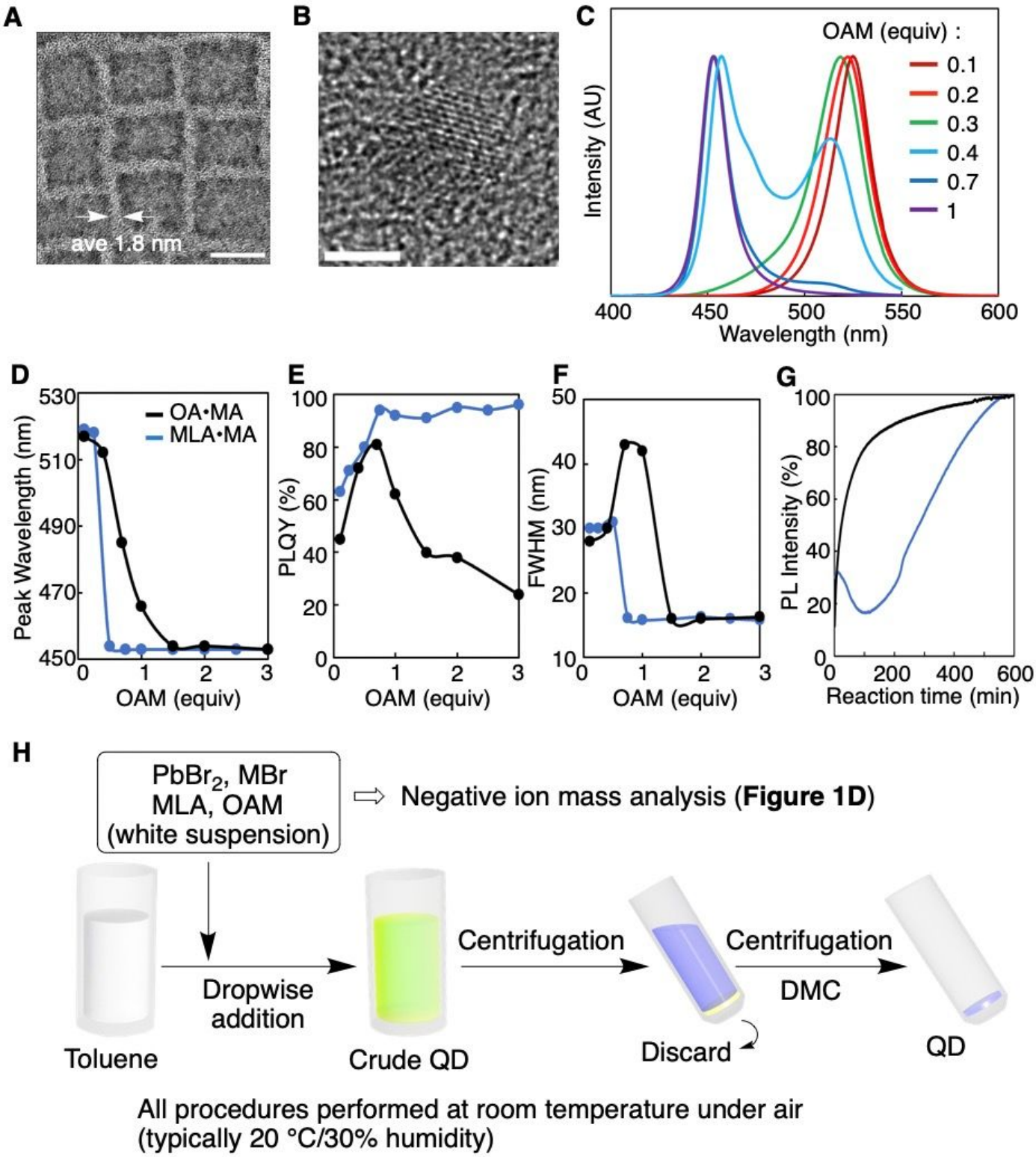

Figure 3

Synthesis and properties of MA•QD made in the presence of a different amount of OAM using OA or MLA. **a**, TEM image of green-emitting colloid of QD particles on aC, made with 0.15 equiv of OAM/$PbBr_2$. Scale bar = 10 nm. **b**, TEM image of **1** made with 1.5 equiv OAM. The reaction was terminated at 3 h after dilution with toluene. Scale bar = 2 nm. **c**, OAM-dependent change of emission wavelength (intensity normalized). **d**, OAM-dependent change of maximum emission wavelength. **e**, Change of PLQY. **f**, Change of FWHM. **g**, Reaction kinetics as monitored at 453 nm by the evolution of the PL intensity through time. The intensity is normalized to the value after 600 min. **h**, Standard procedure including purification with dimethyl carbonate (DMC).

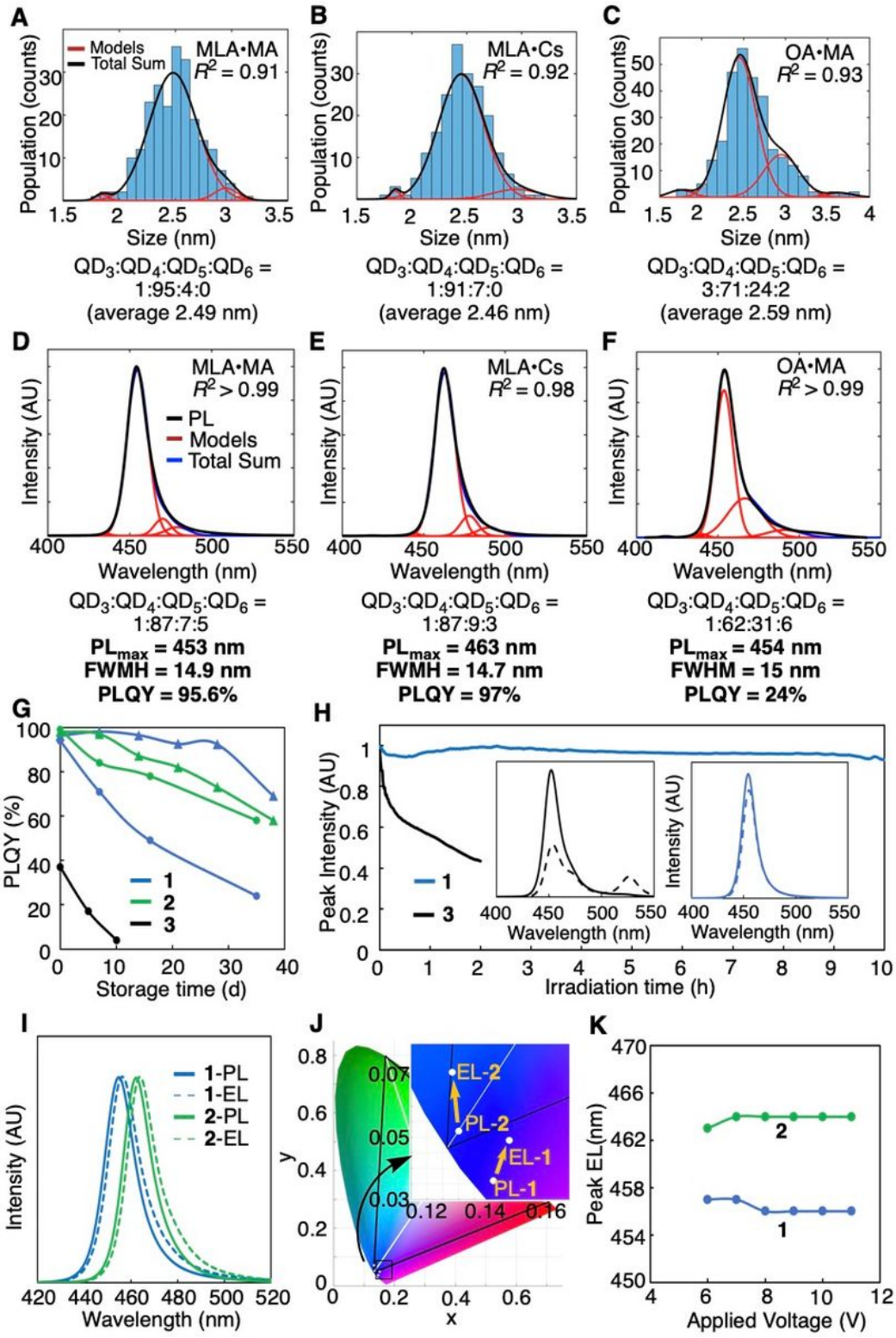

Figure 4

Physical properties of MLA•M•QD_4. **a**–**c**, Diameter distribution and Gaussian regression analysis were performed on many images of **1** (**a**, also shown in Fig. 3b), **2** **b**, and **3** **c**, on aC**. d**–**f**, Emission spectra and Gaussian regression analysis for **1** **d**, **2** **e**, and **3** **f**. **g**, Storage stability in the dark at 5 °C for days. Curves with triangles indicate posttreatment for stabilization by adding 4 mg/mL MLA to the final toluene suspension. **h**, Change of blue emission intensity upon UV irradiation (372 nm). Insets, before (solid line)

and after (broken line) 2 h UV irradiation. **i**, Photoluminescence (solid) and electroluminescence (dots) of **1** and **2**. (**J**) CIE diagram showing photo- (PL) and electroluminescence (EL) of **1** and **2**. **k**, Wavelength shift of EL peak dependent on the applied voltage. Device architecture: ITO/PEDOT:PSS/poly-TPD/QD/TPBi/Ag, see ESM for details.

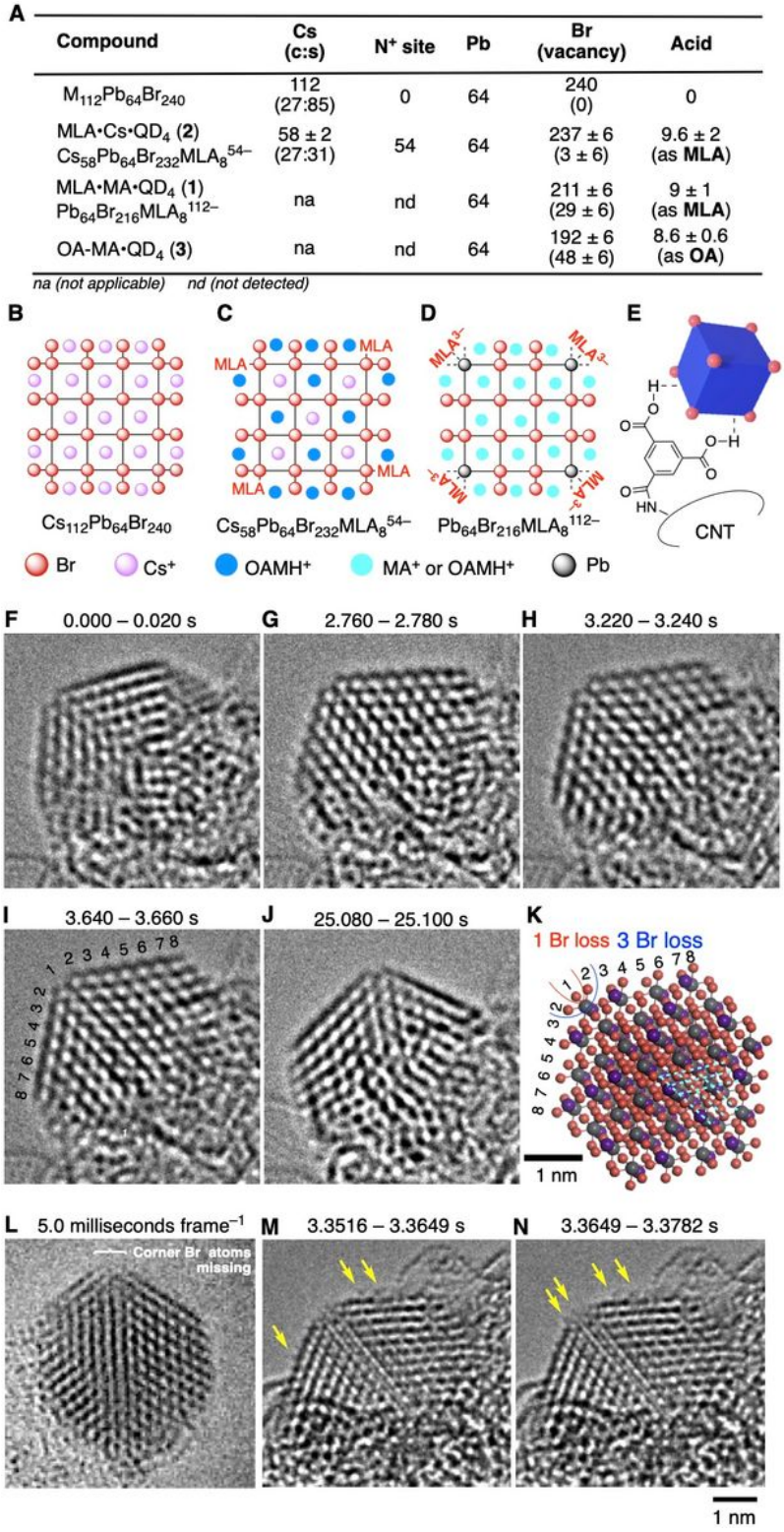

Figure 5

EDX and SMART-EM analysis. a, Elemental composition determined using SEM-EDX. **c:s** indicates central:surface. **N^+** site indicates $OAMH^+$ site. **b**, Side view of the first layer of $Cs_{112}Pb_{64}Br_{240}$. Only the monovalent Br ions are shown for clarity. **c**, **2** based on EDX data in **A**. **d**, **1** based on EDX data. **e**, Model of QD_4 captured on CNT aggregate via 1,3,5-benzenetricarboxylic acid. **f–j**, SMART-EM images of **2** on CNT aggregate (20 milliseconds $frame^{-1}$, arbitrary time scale). Conditions: 298 K, 80 kV, Electron dose rate (EDR) = 2.1–2.8 ´ 10^7 e^- nm^{-2} s^{-1}. Additional pictures can be found in Supplementary Fig. 15-16. **k**, ZC-model of **2** illustrating one Br loss (red) found in **f–j**, and three Br loss (blue) in **l–n**. **l**, A SMART-EM image of a particle of **1** (possibly larger by one layer of the cubic lattice) (5 milliseconds $frame^{-1}$ taken at the beginning of imaging). **m**, **n**, Two consecutive snapshots of another particle of **1** illustrating the motion of Br atoms on the edges, and the Br loss from the corner (13.3 milliseconds $frame^{-1}$). Yellow arrows show Br atoms in motion. Additional pictures can be found in Supplementary Fig. 17. Scale bar = 1 nm.

Supplementary Files

This is a list of supplementary files associated with this preprint. Click to download.

- Movie3.mov
- SMQDNatureNanotechnologyNakamurasubmitted0318.pdf
- Movie2.mov
- Movie1.mov